

Superconducting qubit-oscillator circuit beyond the ultrastrong-coupling regime

Fumiki Yoshihara,^{1,*} Tomoko Fuse,^{1,*} Sahel Ashhab,²
Kosuke Kakuyanagi,³ Shiro Saito,³ and Kouichi Semba^{1,†}

¹*National Institute of Information and Communications Technology,
4-2-1, Nukuikitamachi, Koganei, Tokyo 184-8795, Japan*

²*Qatar Environment and Energy Research Institute,
Hamad Bin Khalifa University, Qatar Foundation, Doha, Qatar*

³*NTT Basic Research Laboratories,
NTT Corporation, 3-1 Morinosato-Wakamiya,
Atsugi, Kanagawa 243-0198, Japan*

Abstract

To control light-matter interaction at the single-quantum level in cavity quantum electrodynamics (cavity-QED)^{1,2} or circuit-QED³⁻⁵, strong coupling between the light and matter components is indispensable. Specifically, the coupling rate g must be larger than the decay rates. If g is increased further and becomes as large as the frequencies of light and matter excitations, the energy eigenstates including the ground state are predicted to be highly entangled⁶. This qualitatively new coupling regime can be called the deep strong-coupling regime⁷. One approach toward the deep strong-coupling regime is to use huge numbers of identical systems⁸⁻¹⁰ to take advantage of ensemble enhancement¹¹. With the emergence of so-called *macroscopic artificial atoms*, superconducting qubits^{12,13} for example, it has become possible for a single artificial atom to realize ultrastrong coupling, where $\hbar g$ exceeds $\sim 10\%$ of the energies of the qubit $\hbar\omega_q$ and the harmonic oscillator $\hbar\omega_o$ ¹⁴⁻¹⁶. By making use of the macroscopic magnetic dipole moment of a flux qubit, large zero-point-fluctuation current of an LC oscillator, and large Josephson inductance of a coupler junction, we have realized circuits in the deep strong-coupling regime, where g/ω_o ranges from 0.72 to 1.34 and $g/\omega_q \gg 1$. Using energy spectroscopy measurements, we have observed unconventional transition spectra between Schrödinger cat-like energy eigenstates¹⁷. These states involve quantum superpositions of Fock states with phase-space displacements of $\pm g/\omega_o$ and remarkably survive with environmental noise. Our results provide a basis for ground-state-based entangled-pair generation and open a new direction in circuit-QED.

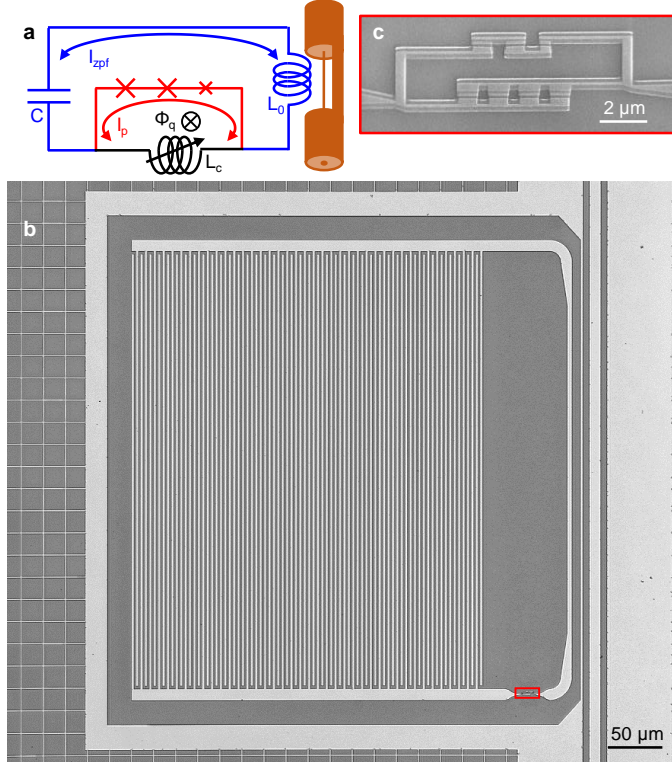


FIG. 1. **Superconducting qubit-oscillator circuit.** **a**, Circuit diagram. A superconducting flux qubit (red and black) and a superconducting LC oscillator (blue and black) are inductively coupled to each other by sharing a tunable inductance (black). **b**, Laser microscope image of the lumped-element LC oscillator inductively coupled to a coplanar transmission line. **c**, Scanning electron microscope (SEM) image of the qubit and the coupler junctions located at the red rectangle in image **b**. The coupler, consisting of four parallel Josephson junctions, is tunable via the magnetic flux bias through its loops (see Methods and Extended Data Fig. 1).

We begin by describing the Hamiltonian of each component in the qubit-oscillator circuit, which comprises a superconducting flux qubit and an LC oscillator inductively coupled to each other by sharing a tunable inductance L_c , as shown in the circuit diagram in Fig. 1a.

The Hamiltonian of the flux qubit can be written in the basis of two states with persistent currents flowing in opposite directions around the qubit loop¹⁸, $|L\rangle_q$ and $|R\rangle_q$, as $\mathcal{H}_q = -\hbar(\Delta\sigma_x + \varepsilon\sigma_z)/2$, where $\hbar\Delta$ and $\hbar\varepsilon$ are the tunnel splitting and the energy bias between $|L\rangle_q$ and $|R\rangle_q$, and $\sigma_{x,z}$ are Pauli matrices. The macroscopic nature of the persistent-current states enables strong coupling to other circuit elements. Another important feature of the flux qubit is its strong anharmonicity: the two lowest energy levels are well isolated from

the higher levels.

The Hamiltonian of the LC oscillator can be written as $\mathcal{H}_o = \hbar\omega_o(\hat{a}^\dagger\hat{a} + 1/2)$, where $\omega_o = 1/\sqrt{(L_0 + L_{qc})C}$ is the resonance frequency, L_0 is the inductance of the superconducting lead, $L_{qc}(\simeq L_c)$ is the inductance across the qubit and coupler (see Methods), C is the capacitance, and $\hat{a}(\hat{a}^\dagger)$ is the oscillator's annihilation (creation) operator. Figure 1b shows a laser microscope image of the lumped-element LC oscillator, where L_0 is designed to be as small as possible to maximize the zero-point fluctuations in the current $I_{zpf} = \sqrt{\hbar\omega_o/2(L_0 + L_{qc})}$ and hence achieve strong coupling to the flux qubit, while C is adjusted so as to achieve a desired value of ω_o . The freedom of choosing L_0 for large I_{zpf} is one of the advantages of lumped-element LC oscillators over coplanar-waveguide resonators for our experiment. Another advantage is that a lumped-element LC oscillator has only one resonant mode. Together with the strong anharmonicity of the flux qubit, we can expect that our circuit will realize the Rabi model^{19–22}, which is one of the simplest possible quantum models of qubit-oscillator systems, with no additional energy levels in the range of interest.

The coupling Hamiltonian can be written as³ $\mathcal{H}_c = \hbar g\sigma_z(\hat{a} + \hat{a}^\dagger)$, where $\hbar g = MI_p I_{zpf}$ is the coupling energy, $M(\simeq L_c)$ is the mutual inductance between the qubit and the LC oscillator, and I_p is the maximum persistent current of the qubit. Importantly, a Josephson-junction circuit is used as a large inductive coupler²³ (Fig. 1c), which together with large I_p and I_{zpf} leads to deep strong coupling.

The total Hamiltonian of the circuit is then given by

$$\mathcal{H}_{\text{total}} = -\frac{\hbar}{2}(\Delta\sigma_x + \varepsilon\sigma_z) + \hbar\omega_o(\hat{a}^\dagger\hat{a} + \frac{1}{2}) + \hbar g\sigma_z(\hat{a} + \hat{a}^\dagger). \quad (1)$$

Nonlinearities in the coupler circuit lead to higher-order terms in $(\hat{a} + \hat{a}^\dagger)$. The leading-order term can be written as $C_{A2}\hbar g(\hat{a} + \hat{a}^\dagger)^2$ and is known as the A^2 term²⁴ in atomic physics. Since this A^2 term can be eliminated from $\mathcal{H}_{\text{total}}$ by a variable transformation (see Methods), we do not explicitly keep it and instead use Eq. (1) for data analysis.

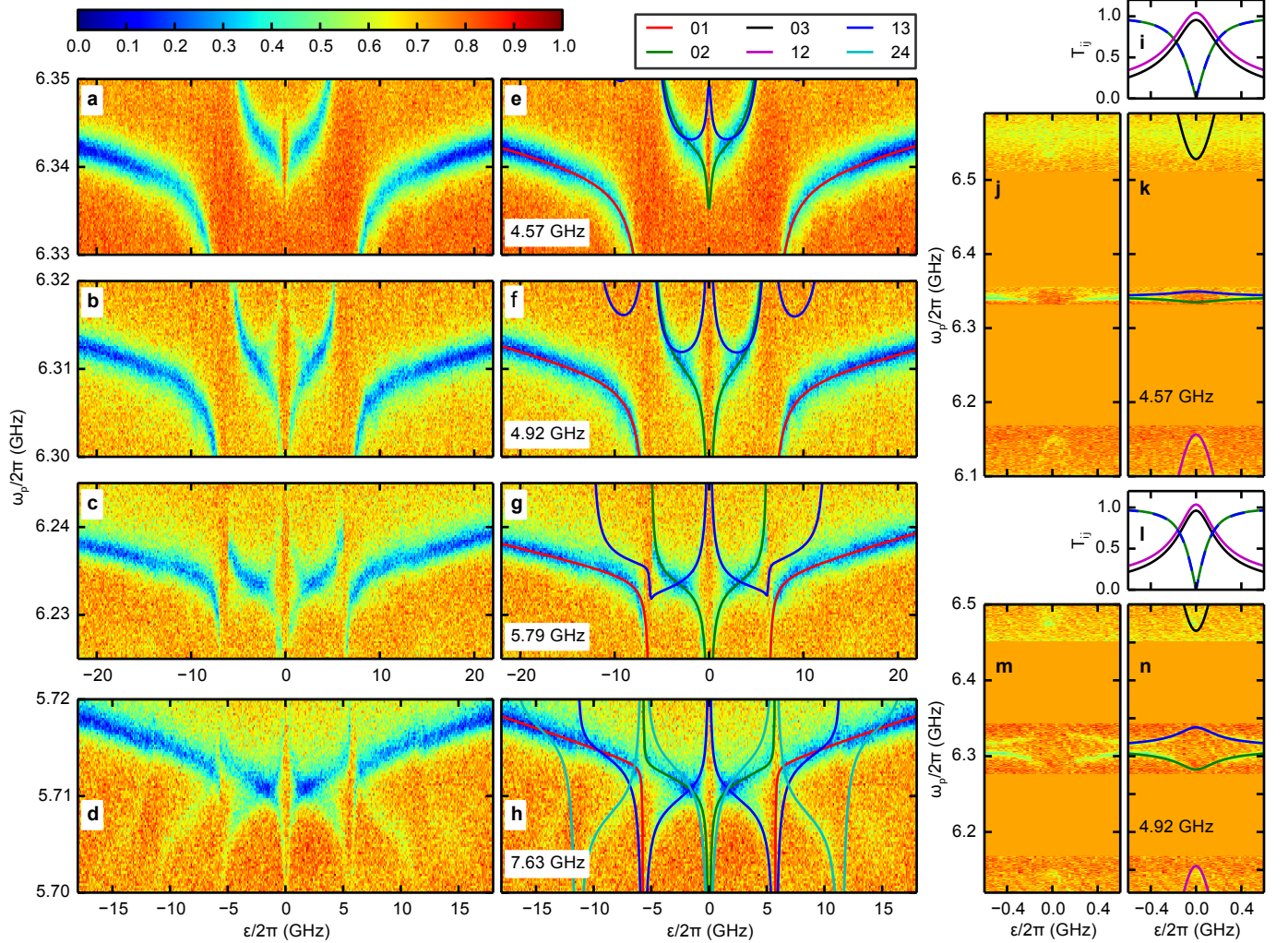


FIG. 2. **The transmission spectra with calculated frequencies and matrix elements of transitions.** **a–d, j, m** (**e–h, k, n**), The normalized amplitude of the transmission spectra (with calculated transition frequencies ω_{ij}^{cal}), and **i, l** the transition matrix elements T_{ij} as functions of flux bias ε . As summarized in Table I, panels **a, e, i, j,** and **k** show data from circuit I at $\Phi_q/\Phi_0 = -0.5$, panels **b, f, l, m,** and **n** show data from circuit I at $\Phi_q/\Phi_0 = -1.5$, panels **c** and **g** show data from circuit I at $\Phi_q/\Phi_0 = 2.5$, and panels **d** and **h** show data from circuit II at $\Phi_q/\Phi_0 = -0.5$. The values of $g/2\pi$ are written in the panels. The red, green, black, magenta, blue, and cyan lines indicate the $|0\rangle \rightarrow |1\rangle$, $|0\rangle \rightarrow |2\rangle$, $|0\rangle \rightarrow |3\rangle$, $|1\rangle \rightarrow |2\rangle$, $|1\rangle \rightarrow |3\rangle$, and $|2\rangle \rightarrow |4\rangle$ transitions, respectively.

Spectroscopy was performed by measuring the transmission spectrum through the coplanar transmission line, which is inductively coupled to the LC oscillator (see Methods and

TABLE I. Set of parameters obtained from spectroscopy measurements.

circuit	Φ_q/Φ_0	Fig. 2	$\Delta/2\pi$ (GHz)	$\omega_o/2\pi$ (GHz)	$g/2\pi$ (GHz)	$\alpha = g/\omega_o$
I	-0.5	a, e, i-k	0.505	6.336	4.57	0.72
I	-1.5	b, f, l-n	0.430	6.306	4.92	0.78
I	2.5	c, g	0.299	6.233	5.79	0.93
II	-0.5	d, h	0.441	5.711	7.63	1.34

The parameters are obtained from four spectroscopy data in two circuits. The column “Fig. 2” shows the corresponding panels in Fig. 2.

Extended Data Fig. 4). For a systematic study of the g dependence, four flux bias points in two circuits were chosen. Figures 2**a–d** show normalized amplitudes of the transmission spectra $|S_{21}(\omega_p)|/|S_{21}(\omega_p)|_{\max}$ as functions of the flux bias ε , where ω_p is the frequency of the probe signal. At each ε , the spectroscopy data was fitted with Lorentzians to obtain the frequencies ω_{ij} of the transitions $|i\rangle \rightarrow |j\rangle$. Theoretical fits to ω_{ij} were obtained by diagonalizing $\mathcal{H}_{\text{total}}$, treating Δ , ω_o , and g as fitting parameters. The obtained parameters are shown in Table I. For all four data sets, $\Delta/2\pi$ and $\omega_o/2\pi$ are around 0.4 GHz and 6 GHz, respectively. The coupling rates g , which are tuned via the flux bias (see Methods), are much larger than Δ and are comparable to ω_o . Importantly, in circuit II, g is larger than both ω_o and Δ , emphasizing that the circuit is in the deep strong-coupling regime [$g \gtrsim \max(\omega_o, \sqrt{\Delta\omega_o}/2)$]¹⁷. Figures 2**e–h** show the calculated transition frequencies ω_{ij}^{cal} superimposed on the measured transmission spectra **a–d**. As g increases, the anticrossing gap between the qubit and the oscillator at $\varepsilon \simeq \pm\omega_o$ becomes smaller and the structure around $\varepsilon = 0$ changes. These features agree well with the data, indicating that the circuit is well described by $\mathcal{H}_{\text{total}}$.

To capture signals from other transitions, the transmission spectra in a wider ω_p range and a smaller ε range were measured, as shown in Figs. 2**j** and **m** (with ω_{ij}^{cal} in **k** and **n**). Around $\varepsilon = 0$, the signals from the $|0\rangle \rightarrow |2\rangle$ and $|1\rangle \rightarrow |3\rangle$ transitions disappear while signals from the $|0\rangle \rightarrow |3\rangle$ and $|1\rangle \rightarrow |2\rangle$ transitions appear near ω_{03}^{cal} and ω_{12}^{cal} . The appearance and

TABLE II. **The energy eigenstates of the qubit-oscillator system.**

energy eigenbasis		qubit⟩ ⊗ oscillator⟩ basis	
$g < \frac{\omega_o}{2}$	$g > \frac{\omega_o}{2}$	arbitrary g	$g = 0$
0⟩	0⟩	$(L\rangle_q \otimes -\alpha\rangle_o + R\rangle_q \otimes \alpha\rangle_o)/\sqrt{2}$	$ g\rangle_q \otimes 0\rangle_o$
1⟩	1⟩	$(L\rangle_q \otimes -\alpha\rangle_o - R\rangle_q \otimes \alpha\rangle_o)/\sqrt{2}$	$ e\rangle_q \otimes 0\rangle_o$
2⟩	3⟩	$(L\rangle_q \otimes \hat{D}(-\alpha) 1\rangle_o + R\rangle_q \otimes \hat{D}(\alpha) 1\rangle_o)/\sqrt{2}$	$ g\rangle_q \otimes 1\rangle_o$
3⟩	2⟩	$(L\rangle_q \otimes \hat{D}(-\alpha) 1\rangle_o - R\rangle_q \otimes \hat{D}(\alpha) 1\rangle_o)/\sqrt{2}$	$ e\rangle_q \otimes 1\rangle_o$

The left two columns are written in the energy eigenbasis while the right two columns are written in the tensor product basis of qubit and oscillator states. The energy eigenstates |2⟩ and |3⟩ cross at $g \simeq \omega_o/2$. $|L\rangle_q$ and $|R\rangle_q$ are the persistent-current states of the qubit, $|g\rangle_q$ and $|e\rangle_q$ are the energy eigenstates of the qubit, $|\pm\alpha\rangle_o = \hat{D}(\pm\alpha)|0\rangle_o$ are coherent states of the oscillator, $\hat{D}(\alpha)$ is a displacement operator, and $|n\rangle_o$ is a Fock state of the oscillator. At $g = 0$ and hence $\alpha = 0$, the energy eigenstates are product states, as shown in the right-most column. For arbitrary g , the energy eigenstates of the qubit-oscillator system are entangled states.

disappearance of the signals are well explained by the transition matrix elements $T_{ij} = \langle i | (\hat{a} + \hat{a}^\dagger) | j \rangle$ shown in Figs. 2i and 1: at $\varepsilon = 0$, $|T_{02}| = |T_{13}| = 0$, while $|T_{03}|$ and $|T_{12}|$ are maximum. This structure is a consequence of the symmetric and antisymmetric quantum superpositions shown in Table II, as we shall discuss below. In circuit I at $\Phi_q/\Phi_0 = -1.5$, both our experimental data and theoretical calculations give $\omega_{01}(\varepsilon = 0)/\Delta = 0.13 \text{ GHz}/0.43 \text{ GHz} = 0.30$, meaning that the Lamb shift²⁵ is 70% of the bare qubit frequency. Signals from the $|0\rangle \rightarrow |3\rangle$ and $|1\rangle \rightarrow |2\rangle$ transitions were not observed in circuit I at $\Phi_q/\Phi_0 = 2.5$ and in circuit II, where the transmission spectra have more noise.

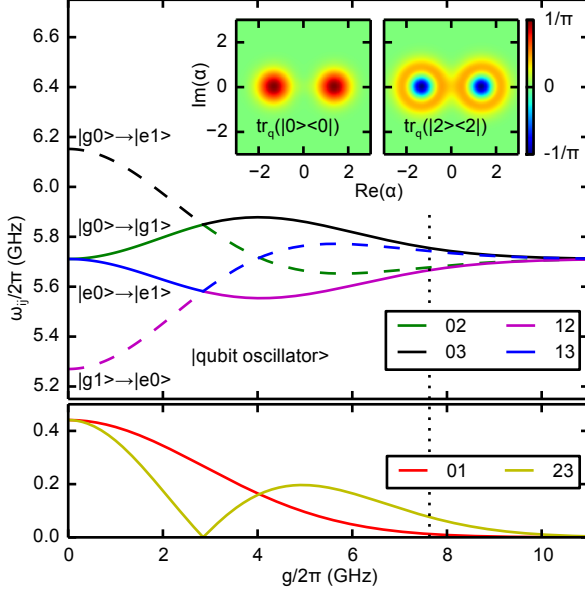


FIG. 3. **Calculated transition frequencies and Wigner functions.** Calculated transition frequencies are plotted as a function of g at $\varepsilon = 0$. The parameters of circuit II, $\Delta/2\pi = 0.441$ GHz and $\omega_o/2\pi = 5.711$ GHz, are chosen. Solid (dashed) lines indicate that the corresponding matrix elements T_{ij} are nonzero (zero). The labels in the ket vector indicate the corresponding transitions at $g = 0$ described as an energy eigenstate of the qubit (e, g) and a Fock state of the oscillator (0, 1). The black dotted line is at the coupling strength in circuit II, $g/2\pi = 7.63$ GHz. The insets show calculated Wigner functions for the reduced density operators of the oscillator at this value of g .

The eigenstates of the qubit-oscillator system in the case $\omega_o \gg \Delta$ can be understood in the following way¹⁷. The state of the oscillator is displaced in one of two opposite directions depending on the persistent-current state of the qubit: $|L\rangle_q \otimes |n\rangle_o \rightarrow |L\rangle_q \otimes \hat{D}(-\alpha)|n\rangle_o$ and $|R\rangle_q \otimes |n\rangle_o \rightarrow |R\rangle_q \otimes \hat{D}(\alpha)|n\rangle_o$. Here, $|n\rangle_o$ is a Fock state associated with n plasmons in the oscillator, $\hat{D}(\alpha) = \exp(\alpha\hat{a}^\dagger - \alpha\hat{a})$ is the displacement operator, and $\alpha = g/\omega_o$ is the displacement given in Table I. As the energy eigenstates of the qubit are superpositions of the persistent-current states, $|g\rangle_q = (|L\rangle_q + |R\rangle_q)/\sqrt{2}$ and $|e\rangle_q = (|L\rangle_q - |R\rangle_q)/\sqrt{2}$, the energy eigenstates of the qubit-oscillator system are well described by the Schrödinger-cat-like entangled states between the persistent-current states of the qubit and displaced Fock states of the oscillator $\hat{D}(\pm\alpha)|n\rangle_o$, as shown in Table II. Note that the coherent state $|\alpha\rangle_o$, the eigenstate of \hat{a} associated with the eigenvalue α , is a displaced vacuum state:

$|\alpha\rangle_o = \hat{D}(\alpha)|0\rangle_o$. In Fig. 3, ω_{ij}^{cal} are plotted as functions of g for the parameters of circuit II, i.e. $\Delta/2\pi = 0.441$ GHz and $\omega_o/2\pi = 5.711$ GHz, at $\varepsilon = 0$. At $g = 0$, $\omega_{02} = \omega_{13} = \omega_o$, $\omega_{12} = \omega_o - \Delta$, and $\omega_{03} = \omega_o + \Delta$. The $|i\rangle_q \otimes |0\rangle_o \leftrightarrow |j\rangle_q \otimes |1\rangle_o$ transition is bright (dark) if $i = j$ ($i \neq j$). At $g \ll \omega_o$, ω_{02} and ω_{13} split as $\omega_{02} \simeq \omega_o + g^2/(\omega_o - \Delta)$ and $\omega_{13} \simeq \omega_o - g^2/(\omega_o - \Delta)^{26}$. As g increases further, the above description of ω_{02} and ω_{13} breaks down, and bright and dark transitions cross at $g/2\pi \simeq \omega_o/4\pi = 2.86$ GHz. In Figs. 2j and m, two dark transitions are located between two bright transitions, which confirms that g is larger than the crossing point at $g \simeq \omega_o/2$.

The insets of Fig. 3 show the Wigner functions²⁷, $W(\alpha, \rho) = (1/\pi^2) \int \exp(\eta^* \alpha - \eta \alpha^*) \text{tr}[\rho \exp(\eta \hat{a}^\dagger - \eta^* \hat{a})] d^2 \eta$, of the reduced density operators of the oscillator $\text{tr}_q(|0\rangle\langle 0|)$ and $\text{tr}_q(|2\rangle\langle 2|)$ in the case of circuit II, where tr_q is the partial trace over qubit states. The states $\text{tr}_q(|0\rangle\langle 0|)$ and $\text{tr}_q(|2\rangle\langle 2|)$ are well described by mixtures of the two coherent states $|\pm \alpha\rangle$ and the two displaced Fock states $\hat{D}(\pm \alpha)|1\rangle$ separated from each other by $2\alpha = 2.67$, which is substantially larger than the width of the vacuum state and gives a ground-state entanglement of 99.88 % (see Methods and Extended Data Fig. 5). This highly entangled ground state can be prepared by letting the system relax to thermal equilibrium at a low temperature. These entangled states are normally thought of as being very fragile. The fact that all the measured lines follow the frequencies and brightness features predicted theoretically, however, indicates that the corresponding entangled states are robust against the decoherence caused by the dissipative processes in the experiment.

The average number of virtual plasmons in the oscillator in the ground state in circuit II is calculated to be $|\alpha|^2 = 1.80$, indicating that the oscillator is in a superradiant state, which contradicts the no-go theorem of the superradiance phase transition²⁴. The condition for the no-go theorem can be expressed as $C_{A2} > g/\Delta$, which is violated in our experiment (see Methods). It should be emphasized here that if there were corrections to the Hamiltonian that correspond to the conditions of the no-go theorem, they would have affected our experimentally obtained parameters such that these parameters satisfy $g < \sqrt{\Delta\omega_o}/2$.

In conclusion, we have experimentally achieved deep-strong coupling between a superconducting flux qubit and an LC oscillator. Our results indicate that the energy eigenstates are Schrödinger-cat-like entangled states between persistent-current states of the qubit and displaced Fock states of the oscillator. We have also observed a huge Lamb shift, 70% of the bare qubit frequency. The tiny Lamb shift in atoms, which arises from weak vacuum

fluctuations, was one of the earliest phenomena to stimulate the study of quantum electrodynamics. Now we can design artificial systems with light-matter interaction so strong that instead of speaking of vacuum fluctuations we speak of a strongly correlated light-matter ground state, defining a new state of matter and opening prospects for applications in quantum technologies.

ACKNOWLEDGMENTS

We thank Kae Nemoto, Masao Hirokawa, Kunihiro Inomata, John W. Munro, Yuichiro Matsuzaki, Motoaki Bamba, and Norikazu Mizuochi for stimulating discussions. We thank also Mikio Fujiwara, Kentaro Wakui, Masahiro Takeoka, and Masahide Sasaki for their continued support through all the stages of this research. We also thank Sander Weinreb and Hamdi Mani for their support by providing excellent cryoamplifiers, and Noriyoshi Matsuura of Agilent Technologies and Yoshitada Kato of Keysight Technologies for their cordial support in the startup phase of this research. This work was supported in part by the Scientific Research (S) Grant No.25220601 by the Japanese Society for the Promotion of Science (JSPS).

AUHTOR CONTRIBUTIONS

All authors contributed extensively to the work presented in this paper. F. Y., T. F., K. S. carried out measurements and data analysis on the coupled flux qubit - LC-oscillaor system. F. Y., T. F. designed and F. Y., T. F., K. K. fabricated the flux-qubit and associated devices. T. F., F. Y., K. K., S. S., and K. S. designed and developed the measurement system. S. A. provided theoretical support and analysis. F. Y., T. F., S. A., and K. S. wrote the manuscript, with feedback from all authors. K. S. designed and supervised the project.

METHODS

Laser microscope image. The laser microscope image in Fig. 1b was obtained by Keyence VK-9710 Color 3D Laser Scanning Microscope. The magnification of the objective lens is 10. The application “VK Viewer” was used for image acquisition.

Scanning electron microscope image. The scanning electron microscope (SEM) image in Fig. 1c was obtained by JEOL JIB-4601F. The acceleration voltage was 10 kV, the magnification was 6500, and the working distance was 8.7 mm.

Flux bias dependence of the critical current of the coupler. The circuit diagram of the coupler in circuit I is shown as the black part of the circuit in Extended Data Fig. 1a. Here, n_{ϕ_c} is the normalized flux bias in units of the superconducting flux quantum $\Phi_0 = h/2e$ through each coupler loop defined by two neighboring parallel junctions. The critical currents of the two large junctions of the flux qubit and the four junctions of the coupler are all equal, with the value I_c . The current through the coupler I_{coup} is the sum of the currents across the four Josephson junctions: $I_{\text{coup}} = I_c(\sin \varphi_a + \sin \varphi_b + \sin \varphi_c + \sin \varphi_d)$, where φ_i ($i = a, b, c, d$) is the phase across junction i . Considering the fluxoid quantization of each loop, the phases can be written using φ_a and n_{ϕ_c} as

$$\varphi_b = \varphi_a + 2\pi n_{\phi_c}, \quad (2)$$

$$\varphi_c = \varphi_a + 4\pi n_{\phi_c}, \quad (3)$$

and

$$\varphi_d = \varphi_a + 6\pi n_{\phi_c}. \quad (4)$$

Here, we ignore the sum of the kinetic and geometric inductances of the superconducting lead, which is at least an order of magnitude smaller than those of the Josephson junctions.

Using Eqs. (2)–(4), I_{coup} can be written as

$$\begin{aligned} I_{\text{coup}} &= I_c[\sin \varphi_a + \sin(\varphi_a + 2\pi n_{\phi_c}) + \sin(\varphi_a + 4\pi n_{\phi_c}) + \sin(\varphi_a + 6\pi n_{\phi_c})] \\ &= 2I_c[\sin(\varphi_a + \pi n_{\phi_c}) \cos(\pi n_{\phi_c}) + \sin(\varphi_a + 5\pi n_{\phi_c}) \cos(\pi n_{\phi_c})] \\ &= 4I_c \sin(\varphi_a + 3\pi n_{\phi_c}) \cos(2\pi n_{\phi_c}) \cos(\pi n_{\phi_c}). \end{aligned} \quad (5)$$

Thus, the critical current of the coupler $I_{c(\text{coup})}$ can be described by the ratio

$$a_c(n_{\phi_c}) = \frac{I_{c(\text{coup})}}{I_c} = 4 \cos(2\pi n_{\phi_c}) \cos(\pi n_{\phi_c}). \quad (6)$$

Now, the coupler junctions in Extended Data Fig. 1a can be replaced by a single effective Josephson junction whose critical current is $a_c(n_{\phi_c})I_c$ as shown in Extended Data Fig. 1b. Circuit II is almost the same as circuit I except that its coupler consists of two Josephson junctions of critical current I_c , forming a superconducting quantum interference device (SQUID). The critical-current ratio of the SQUID is described by

$$a_{c\text{II}}(n_{\phi_{c\text{II}}}) = 2 \cos(\pi n_{\phi_{c\text{II}}}), \quad (7)$$

where $n_{\phi_{c\text{II}}}$ is the normalized flux bias through the SQUID loop. Thus, the circuit diagram of the flux qubit in circuit II is also described by Extended Data Fig. 1b.

Estimation of L_{qc} and M . The circuit in Extended Data Fig. 1b should be simplified to the one in Extended Data Fig. 1c to estimate L_{qc} and M as functions of the bias current δI and normalized flux bias through the qubit loop n_{ϕ_q} in units of Φ_0 . The total Josephson energy of the circuit is given by

$$E_J^{\text{total}} = -E_J [\cos \varphi_1 + \cos \varphi_2 + a_3 \cos \varphi_3 + a_c \cos(-\varphi_u + 2\pi n_{\phi_q})] - \frac{\delta I \Phi_0}{2\pi} \varphi_x, \quad (8)$$

where $E_J = \Phi_0 I_c / 2\pi$, φ_i ($i = 1, 2, 3$) is the phase difference across the i th junction, a_3 and a_c are the critical current ratios of the third and the coupler junctions, $\varphi_u = \varphi_1 + \varphi_2 + \varphi_3$ is the phase difference across the upper branch of the qubit loop, and $\varphi_x = (\varphi_u + \pi n_{\phi_q})$ is the average phase difference across the upper and lower branches of the qubit loop. The last term is the energy of the bias current source.

At $n_{\phi_q} \sim 0.5$, E_J^{total} has two local minima in the three-dimensional parameter space spanned by φ_1 , φ_2 , and φ_3 . The localized state at each minimum corresponds to one of the two persistent-current states of the flux qubit, $|L\rangle_q$ and $|R\rangle_q$. For simplicity, we use the sets of phases $\{\varphi_i^{|L}\rangle\}$ and $\{\varphi_i^{|R}\rangle\}$ at the minima of E_J^{total} as the values of the different phases for $|L\rangle_q$ and $|R\rangle_q$. Extended Data Figure 2a shows the n_{ϕ_q} dependence of different phases corresponding to $|L\rangle_q$ and $|R\rangle_q$. In the calculation, the parameters $I_c = 460$ nA and $a_3 = 0.705$, which are estimated from other samples fabricated simultaneously in the same fabrication process, are used. We also assume that the global magnetic field simultaneously provides flux bias through the loops of the qubit and the coupler according to their area ratio as $n_{\phi_q} : n_{\phi_c} = 24 : 1$.

The qubit-state-dependent inductance across the qubit and coupler $L_{\text{qc}}^{|\text{L(R)}\rangle}$ is calculated considering the Josephson inductances, $L_{\text{J1}}^{|\text{L(R)}\rangle} = \Phi_0/(2\pi I_c \cos \varphi_1^{|\text{L(R)}\rangle})$, $L_{\text{J2}}^{|\text{L(R)}\rangle} = \Phi_0/(2\pi I_c \cos \varphi_2^{|\text{L(R)}\rangle})$, $L_{\text{J3}}^{|\text{L(R)}\rangle} = \Phi_0/(2\pi a_3 I_c \cos \varphi_3^{|\text{L(R)}\rangle})$, and $L_{\text{J4}}^{|\text{L(R)}\rangle} = \Phi_0/(2\pi a_c I_c \cos \varphi_4^{|\text{L(R)}\rangle})$, as

$$L_{\text{qc}}^{|\text{L(R)}\rangle} = \frac{L_{\text{J4}}^{|\text{L(R)}\rangle} (L_{\text{J1}}^{|\text{L(R)}\rangle} + L_{\text{J2}}^{|\text{L(R)}\rangle} + L_{\text{J3}}^{|\text{L(R)}\rangle})}{L_{\text{J1}}^{|\text{L(R)}\rangle} + L_{\text{J2}}^{|\text{L(R)}\rangle} + L_{\text{J3}}^{|\text{L(R)}\rangle} + L_{\text{J4}}^{|\text{L(R)}\rangle}}. \quad (9)$$

Extended Data Figure 2d shows the flux-bias dependence of $L_{\text{qc}}^{|\text{L}\rangle}$ and $L_{\text{qc}}^{|\text{R}\rangle}$, which can be approximately described as $L_{\text{qc}}^{|\text{L}\rangle} = L_{\text{qc0}} + D_{\text{L}}^{|\text{L}\rangle} (n_{\phi_{\text{q}}} - 0.5)$ and $L_{\text{qc}}^{|\text{R}\rangle} = L_{\text{qc0}} - D_{\text{L}}^{|\text{R}\rangle} (n_{\phi_{\text{q}}} - 0.5)$ ($D_{\text{L}}^{|\text{L}\rangle} \sim D_{\text{L}}^{|\text{R}\rangle} < 0$), respectively. The small asymmetry between $L_{\text{qc}}^{|\text{L}\rangle}$ and $L_{\text{qc}}^{|\text{R}\rangle}$ is due to the flux-bias dependence of $a_c(n_{\phi_c})$. Note that at $n_{\phi_{\text{q}}} = 0.5$, $L_{\text{qc}}^{|\text{L}\rangle} = L_{\text{qc}}^{|\text{R}\rangle} = L_{\text{qc0}}$. The inductances of the coupler junction, $L_c^{|\text{L(R)}\rangle} = L_{\text{J4}}^{|\text{L(R)}\rangle}$ are also plotted in Extended Data Fig. 2d, and are slightly larger than $L_{\text{qc}}^{|\text{L(R)}\rangle}$.

It is more convenient to describe the qubit-state-dependent inductance using the energy eigenstates of the qubit, $|\text{g}\rangle_{\text{q}}$ and $|\text{e}\rangle_{\text{q}}$, as

$$\begin{aligned} L_{\text{qc}} &= \frac{1}{2}(L_{\text{qc}}^{|\text{g}\rangle} + L_{\text{qc}}^{|\text{e}\rangle}) + \frac{1}{2}(L_{\text{qc}}^{|\text{g}\rangle} - L_{\text{qc}}^{|\text{e}\rangle})\sigma_z^{\text{eig}} \\ &= \frac{1}{2}(L_{\text{qc}}^{|\text{g}\rangle} + L_{\text{qc}}^{|\text{e}\rangle}) + \frac{1}{2}(L_{\text{qc}}^{|\text{g}\rangle} - L_{\text{qc}}^{|\text{e}\rangle})(\cos \theta \sigma_z + \sin \theta \sigma_x), \end{aligned} \quad (10)$$

where σ_z^{eig} is Pauli matrix in the energy eigenbasis, $\sigma_{x,z}$ are Pauli matrices in the persistent-current basis, θ is defined as $\cos \theta = \varepsilon/\sqrt{\Delta^2 + \varepsilon^2}$, and $L_{\text{qc}}^{|\text{g(e)}\rangle}$ is the inductance across the qubit and the coupler when the qubit state is $|\text{g(e)}\rangle_{\text{q}}$. The relation between the persistent-current states and the energy eigenstates of the qubit is written as

$$\begin{pmatrix} |\text{g}\rangle_{\text{q}} \\ |\text{e}\rangle_{\text{q}} \end{pmatrix} = \begin{pmatrix} \cos \frac{\theta}{2} & \sin \frac{\theta}{2} \\ \sin \frac{\theta}{2} & -\cos \frac{\theta}{2} \end{pmatrix} \begin{pmatrix} |\text{L}\rangle_{\text{q}} \\ |\text{R}\rangle_{\text{q}} \end{pmatrix}. \quad (11)$$

Thus $L_{\text{qc}}^{|\text{L(R)}\rangle}$ can be transformed to $L_{\text{qc}}^{|\text{g(e)}\rangle}$ as

$$\begin{pmatrix} L_{\text{qc}}^{|\text{g}\rangle} \\ L_{\text{qc}}^{|\text{e}\rangle} \end{pmatrix} = \begin{pmatrix} \cos^2 \frac{\theta}{2} & \sin^2 \frac{\theta}{2} \\ \sin^2 \frac{\theta}{2} & \cos^2 \frac{\theta}{2} \end{pmatrix} \begin{pmatrix} L_{\text{qc}}^{|\text{L}\rangle} \\ L_{\text{qc}}^{|\text{R}\rangle} \end{pmatrix}. \quad (12)$$

$L_{\text{qc}}^{|\text{L(R)}\rangle}$ and $L_{\text{qc}}^{|\text{g(e)}\rangle}$ are shown in Extended Data Fig. 3 as functions of the energy bias ε : $L_{\text{qc}}^{|\text{L}\rangle}$ and $L_{\text{qc}}^{|\text{R}\rangle}$ are straight lines, while $L_{\text{qc}}^{|\text{g}\rangle}$ and $L_{\text{qc}}^{|\text{e}\rangle}$ are Λ -shaped and V-shaped, respectively.

Note that the resonance frequency of the LC oscillator $\omega_o = \frac{1}{\sqrt{(L_o+L_{qc})C}}$ also depends on the qubit state and the flux bias via L_{qc} except at $\varepsilon = 0$.

The mutual inductance between the qubit loop and the LC oscillator M can be calculated as $M = \Phi_0 |\delta n_{\phi_q} / \delta I|$, where $(\partial \varphi_u / \partial n_{\phi_q}) \delta n_{\phi_q} = [\varphi_u(\delta I) - \varphi_u(-\delta I)]/2$. The phase φ_u for $|L\rangle$ ($|R\rangle$) as a function of n_{ϕ_q} at $\delta I = \pm 10$ nA are shifted from that at $\delta I = 0$ as shown in Extended Data Fig. 2b (c). From the shifts, M is obtained as shown in Extended Data Fig. 2d. M is found to be very close to the coupler inductance L_c . The flux bias dependence of $a_c(n_{\phi_c})$ causes a small difference in M between two cases of $|L\rangle_q$ and $|R\rangle_q$, which is less than 1 % and we ignore it in the analysis in the main text and the following consideration of the nonlinearity of M .

Nonlinearity of M and the A^2 term of the total Hamiltonian. We consider the nonlinearity of the mutual inductance M between the flux qubit and the LC oscillator. As discussed in the previous section, M is almost the same as L_c , which depends on the current flowing through the Josephson junction I_b as $L_c(I_b) = \Phi_0 / (2\pi \sqrt{(a_c I_c)^2 - I_b^2})$. We thus assume that M can be written in the same way as

$$M(I_b) = \frac{\Phi_0}{2\pi \sqrt{I_{cM}^2 - I_b^2}}, \quad (13)$$

where $I_{cM} = a_c I_c$. The nonlinearity of $M(I_b)$ up to second order in δI_b can be written as

$$\begin{aligned} M(I_b + \delta I_b) &= M(I_b) + \delta I_b \frac{\partial M(I_b)}{\partial I_b} + \frac{\delta I_b^2}{2} \frac{\partial^2 M(I_b)}{\partial I_b^2} \\ &= M(I_b) \left(1 + \frac{I_b \delta I_b}{I_{cM}^2 - I_b^2} + \frac{I_{cM}^2 + 2I_b^2}{2(I_{cM}^2 - I_b^2)^2} \delta I_b^2 \right). \end{aligned} \quad (14)$$

The coupling Hamiltonian can be written as $\mathcal{H}_c = M(\hat{I}_q + \hat{I}_o) \hat{I}_q \hat{I}_o = M(\hat{I}_q + \hat{I}_o) I_p \sigma_z I_{zpf} (\hat{a} + \hat{a}^\dagger)$, where $\hat{I}_q = I_p \sigma_z$ is the persistent-current operator of the qubit, $\hat{I}_o = I_{zpf} (\hat{a} + \hat{a}^\dagger)$ is the zero-point-fluctuation-current operator of the oscillator, and the current $\hat{I}_q + \hat{I}_o$ flows through the mutual inductance. Typically, $I_p \gg I_{zpf}$. Taking into account the nonlinearity of $M(\hat{I}_q + \hat{I}_o)$, the coupling Hamiltonian is written as

$$\begin{aligned}
\mathcal{H}_c &= M(\hat{I}_q + \hat{I}_o)\hat{I}_q\hat{I}_o \\
&= M(\hat{I}_q) \left(1 + \frac{\hat{I}_q\hat{I}_o}{I_{\text{cM}}^2 - \hat{I}_q^2} + \frac{I_{\text{cM}}^2 + 2\hat{I}_q^2}{2(I_{\text{cM}}^2 - \hat{I}_q^2)^2}\hat{I}_o^2 \right) \hat{I}_q\hat{I}_o \\
&= M(I_p) \left[I_p I_{\text{zpf}} \sigma_z (\hat{a} + \hat{a}^\dagger) + \frac{I_p^2 I_{\text{zpf}}^2}{I_{\text{cM}}^2 - I_p^2} (\hat{a} + \hat{a}^\dagger)^2 + \frac{(I_{\text{cM}}^2 + 2I_p^2) I_p I_{\text{zpf}}^3}{2(I_{\text{cM}}^2 - I_p^2)^2} \sigma_z (\hat{a} + \hat{a}^\dagger)^3 \right] \\
&= \hbar g [\sigma_z (\hat{a} + \hat{a}^\dagger) + C_{A2} (\hat{a} + \hat{a}^\dagger)^2 + C_{A3} \sigma_z (\hat{a} + \hat{a}^\dagger)^3], \tag{15}
\end{aligned}$$

where

$$g = M(I_p) I_p I_{\text{zpf}}, \tag{16}$$

$$C_{A2} = \frac{I_p I_{\text{zpf}}}{I_{\text{cM}}^2 - I_p^2}, \tag{17}$$

and

$$C_{A3} = \frac{(I_{\text{cM}}^2 + 2I_p^2) I_{\text{zpf}}^2}{2(I_{\text{cM}}^2 - I_p^2)^2}. \tag{18}$$

Here, we consider terms up to second order in I_{zpf}/I_p . We find that $1 \gg C_{A2} \gg C_{A3}$ considering the following relation, $I_{\text{cM}} (= a_c I_c) > I_p (\lesssim a_3 I_c) \gg I_{\text{zpf}} (\ll I_c)$, where a_c is given in Eqs. (6) or (7), $0.4 \lesssim a_3 \lesssim 0.8$, I_c is several hundred nano amperes, and I_{zpf} is several ten nano amperes. Since the term C_{A3} is very small, we ignore the third term in Eq. (15).

The total Hamiltonian of the circuit considering the nonlinearity of M up to first order in I_{zpf}/I_p is given by

$$\mathcal{H}_{\text{total}} = -\frac{\hbar}{2}(\Delta\sigma_x + \varepsilon\sigma_z) + \hbar\omega_o \left(\hat{a}^\dagger\hat{a} + \frac{1}{2} \right) + \hbar g \sigma_z (\hat{a} + \hat{a}^\dagger) + C_{A2} \hbar g (\hat{a} + \hat{a}^\dagger)^2, \tag{19}$$

where the first term is the Hamiltonian of the flux qubit, the second term is the Hamiltonian of the LC oscillator, and the third term is the coupling Hamiltonian. The fourth term proportional to $(\hat{a} + \hat{a}^\dagger)^2$ is known as the A^2 term in atomic physics. This term can be eliminated by a variable transformation as

$$\begin{aligned}
\mathcal{H}_{\text{total}} &= -\frac{\hbar}{2}(\Delta\sigma_x + \varepsilon\sigma_z) + \hbar\omega_o \left(\hat{a}^\dagger \hat{a} + \frac{1}{2} \right) + C_{A2} \hbar g (\hat{a} + \hat{a}^\dagger)^2 + \hbar g \sigma_z (\hat{a} + \hat{a}^\dagger) \\
&= -\frac{\hbar}{2}(\Delta\sigma_x + \varepsilon\sigma_z) + \left(\frac{\hbar\omega_o}{4} + C_{A2} \hbar g \right) (\hat{a} + \hat{a}^\dagger)^2 - \frac{\hbar\omega_o}{4} (\hat{a} - \hat{a}^\dagger)^2 + \hbar g \sigma_z (\hat{a} + \hat{a}^\dagger) \\
&= -\frac{\hbar}{2}(\Delta\sigma_x + \varepsilon\sigma_z) + \frac{\hbar\omega'_o}{4} (\hat{b} + \hat{b}^\dagger)^2 - \frac{\hbar\omega'_o}{4} (\hat{b} - \hat{b}^\dagger)^2 + \hbar g' \sigma_z (\hat{b} + \hat{b}^\dagger) \\
&= -\frac{\hbar}{2}(\Delta\sigma_x + \varepsilon\sigma_z) + \hbar\omega'_o \left(\hat{b}^\dagger \hat{b} + \frac{1}{2} \right) + \hbar g' \sigma_z (\hat{b} + \hat{b}^\dagger), \tag{20}
\end{aligned}$$

where

$$\omega'_o = \sqrt{\omega_o^2 + 4C_{A2}g\omega_o}, \tag{21}$$

$$g' = \sqrt{\frac{\omega_o}{\omega'_o}} g, \tag{22}$$

and the new field operators,

$$\hat{b} + \hat{b}^\dagger = \sqrt{\frac{\omega'_o}{\omega_o}} (\hat{a} + \hat{a}^\dagger) \tag{23}$$

and

$$\hat{b} - \hat{b}^\dagger = \sqrt{\frac{\omega_o}{\omega'_o}} (\hat{a} - \hat{a}^\dagger), \tag{24}$$

are used. The form of the Hamiltonian in Eq. (20) is exactly the same as the one with the term linear in $(\hat{a} + \hat{a}^\dagger)$, which is given by

$$\mathcal{H}_{\text{total}}^{\text{linear}} = -\frac{\hbar}{2}(\Delta\sigma_x + \varepsilon\sigma_z) + \hbar\omega_o \left(\hat{a}^\dagger \hat{a} + \frac{1}{2} \right) + \hbar g \sigma_z (\hat{a} + \hat{a}^\dagger). \tag{25}$$

Note that the transformation described by Eqs. (23) and (24) is a Hopfield-Bogoliubov transformation²⁸. It guarantees that $[\hat{b}, \hat{b}^\dagger] = [\hat{a}, \hat{a}^\dagger] = 1$. In other words, both the \hat{a} operators and the \hat{b} operators obey the harmonic oscillator commutation relations. The two sets of operators are related to each other by quadrature squeezing operations. The most natural choice among these, and all other quadrature-squeezed variants, is the one that leads to the standard form of the harmonic oscillator Hamiltonian, usually expressed as $\hbar\omega_o \hat{a}^\dagger \hat{a}$. As such, the \hat{b} operators are the most natural oscillator operators for our circuits. The \hat{a} operators

were defined based on an incomplete description of the circuit, considering the properties of the LC circuit and ignoring the qubit and coupler parts of the circuit. In particular, the A^2 term in our circuits describes an additional contribution to the inductive energy of the oscillator that arises in the presence of the qubit and coupler circuits. Similarly, the expression given in the main text for the current zero-point fluctuations must be modified in order to correctly describe the fluctuations in the full circuit.

Condition for superradiant phase transition. In cases where one expects a sharp transition from a normal to a superradiant state, e.g. when $\Delta \gg \omega_o$ or when the single qubit is replaced by a large ensemble of N qubits (and g is defined to include the ensemble enhancement factor \sqrt{N}), the phase transition condition (without the A^2 term) is:

$$4g^2 = \Delta \times \omega_o. \quad (26)$$

After taking into account the renormalization of ω_o and g caused by the A^2 term, the condition for the phase transition becomes

$$4g^2 \sqrt{\frac{\omega_o}{\omega_o + 4C_{A2}g}} = \Delta \times \omega_o \times \sqrt{\frac{\omega_o + 4C_{A2}g}{\omega_o}}, \quad (27)$$

or in other words

$$4g^2 = \Delta \times (\omega_o + 4C_{A2}g). \quad (28)$$

If the parameters are constrained to satisfy the relation $C_{A2} > g/\Delta$, the right-hand side increases whenever we increase the left-hand side, and no matter how large g becomes it will never be strong enough to satisfy the phase transition condition. This can indeed be the case with atomic qubits, and it leads to the no-go theorem in those systems²⁴.

Measurement setup. The energy spectroscopy of the qubit coupled to the LC oscillator is performed via the coplanar transmission line, which is inductively coupled to the LC oscillator, as shown in Extended Data Fig. 4. The probe microwave signal is continuous, sent from a network analyser (Agilent N5234A), and attenuated in the signal input line before arriving at the sample, which is placed in a magnetic shield. The transmitted signal from the sample is amplified (by Caltech cryogenic LNA model CITCRYO4-12A) and measured by the network analyser. When the frequency of the probe signal ω_p matches the frequency of a transition between two energy levels, the transmission amplitude decreases, provided that the transition matrix element is not zero. The input power is kept as low as possible to avoid cascade transitions, such as the transition $|i\rangle \rightarrow |j\rangle$ followed by $|j\rangle \rightarrow |k\rangle$ when

$\omega_p \simeq \omega_{ij} \simeq \omega_{jk}$. The samples are measured in a dilution refrigerator with a base temperature of 10 mK, which corresponds to about 0.2 GHz in frequency. This frequency is slightly higher than $\omega_{01}/2\pi (\simeq 0.13 \text{ GHz})$ in circuit I at $\Phi_q = -1.5\Phi_0$, but lower than all other relevant transitions. Therefore, in thermal equilibrium the states $|0\rangle$ and $|1\rangle$ are partly occupied, with respective probabilities 0.65 and 0.35, and the occupation probabilities of the higher excited states are negligible. In Fig. 2 in the main text, the transmission spectrum $S_{21}(\omega_p)$ is measured at each flux bias ε , and $|S_{21}(\omega_p, \varepsilon)|$ is shown.

Evaluation of qubit-oscillator entanglement. The qubit-oscillator entanglement in the ground state can be estimated using the approximate expression for the state

$$|0\rangle = \frac{1}{\sqrt{2}} \left(|L\rangle_q \otimes |-\alpha\rangle_o + |R\rangle_q \otimes |\alpha\rangle_o \right). \quad (29)$$

Taking into consideration the fact that $\langle \alpha | -\alpha \rangle = e^{-2\alpha^2}$, the qubit's reduced density matrix is given by

$$\rho_q = \frac{1}{2} \begin{pmatrix} 1 & e^{-2\alpha^2} \\ e^{-2\alpha^2} & 1 \end{pmatrix}. \quad (30)$$

The eigenvalues of ρ_q are then $(1 \pm e^{-2\alpha^2})/2$. The entanglement can now be evaluated as the (base-2) von Neumann entropy of the qubit:

$$\begin{aligned} S &= -\text{Tr}\{\rho_q \log_2 \rho_q\} \\ &= -\frac{1}{2} \left(1 + e^{-2\alpha^2}\right) \log_2 \left(\frac{1 + e^{-2\alpha^2}}{2}\right) - \frac{1}{2} \left(1 - e^{-2\alpha^2}\right) \log_2 \left(\frac{1 - e^{-2\alpha^2}}{2}\right), \end{aligned} \quad (31)$$

which when expanded to second order in $e^{-2\alpha^2}$ gives

$$S = 1 - \frac{1}{2 \ln 2} e^{-4\alpha^2}. \quad (32)$$

Extended Data Figure 5 shows the entanglement calculated based on the approximate expression for the ground state Eq. (29), with and without the small $e^{-2\alpha^2}$ approximation, along with the entanglement obtained for the numerically calculated (and essentially exact) ground state. For the parameters of circuit II, Eqs. (31) and (32) give an entanglement of 99.94% while the exact calculation gives the value 99.88%.

Equation (32) is a poor approximation for $\alpha < 0.5$, because when we expanded the logarithm in a Taylor series we assumed a small value of $e^{-2\alpha^2}$. Figure 5 suggests that Eqs. (31) and (32) deviate from the exact result for $\alpha > 1.5$ as well. It should be noted,

however, that the absolute value of the error in these approximate expressions decreases monotonically and approaches zero as $\alpha \rightarrow \infty$. It is only when the error is compared to the rapidly decreasing quantity $1 - S$ that the approximate expressions seem to deviate from the exact result for large values of α .

It can also be seen in Fig. 5 that the approximate expression Eq. (29) leads to an overestimation of the entanglement. This overestimation is due to the fact that Eq. (29) is obtained by ignoring the σ_x term in the Hamiltonian (except for its role in identifying the symmetric superposition as the ground state of the coupled system). Because this term does not contain oscillator operators, it favours having a superposition of the states $|L\rangle_q$ and $|R\rangle_q$ with the state of the oscillator being independent of the state of the qubit. It therefore favours a slightly increased overlap (in the state of the oscillator) between the two branches of the superposition than the overlap present in Eq. (29), and the increased overlap leads to a reduction in the entanglement.

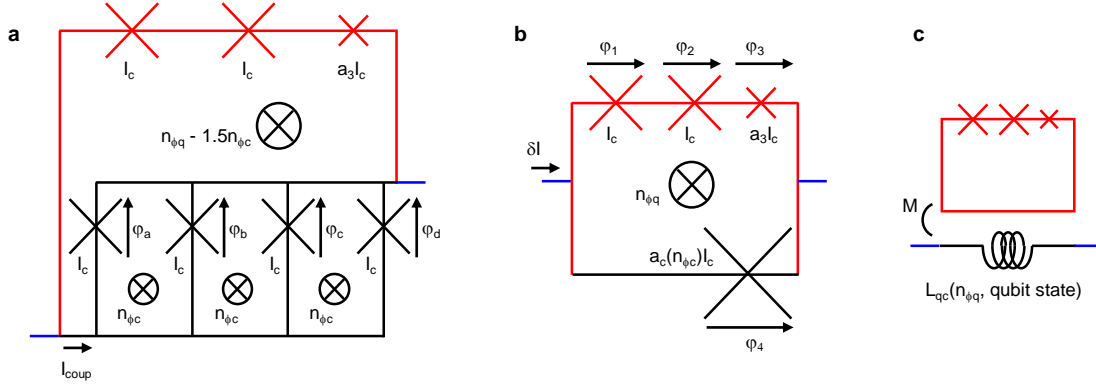
* These authors contributed equally to this work.

† semba@nict.go.jp

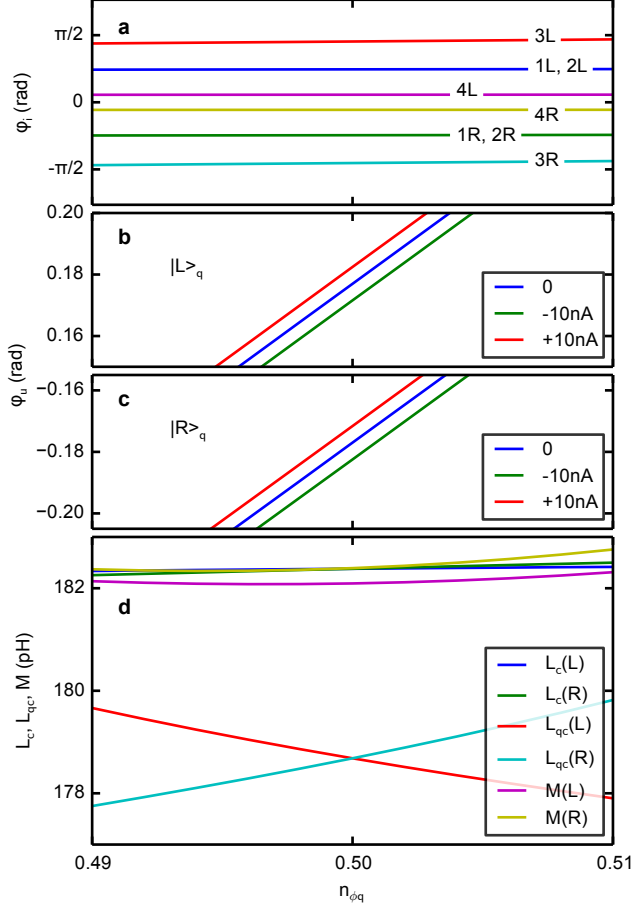
- ¹ Brune, M. *et al.* Quantum Rabi Oscillation: A Direct Test of Field Quantization in a Cavity. *Phys. Rev. Lett.* **76**, 1800–1803 (1996).
- ² Wineland, D. J. & Itano, W. M. Spectroscopy of a single Mg⁺ ion. *Phys. Lett. A* **82(2)**, 75–78 (1981).
- ³ Chiorescu, I. *et al.* Coherent dynamics of a flux qubit coupled to a harmonic oscillator. *Nature* (London) **431**, 159–162 (2004).
- ⁴ Wallraff, A. *et al.* Strong coupling of a single photon to a superconducting qubit using circuit quantum electrodynamics. *Nature* (London) **431**, 162–167 (2004).
- ⁵ Viennot, J. J., Dartiailh, M. C., Cottet, A. & Kontos, T. Coherent coupling of a single spin to microwave cavity photons. *Science* **349**, 408–411 (2015).
- ⁶ Hepp, K. & Lieb, E. H. On the Superradiant Phase Transition for Molecules in a Quantized Radiation Field : the Dicke Maser Model. *Ann. Phys. (NY)* **76**, 360–404 (1973).
- ⁷ Casanova, J., Romero, G., Lizuain, I., Garca-Ripoll, J. J. & Solano, E. Deep Strong Coupling Regime of the Jaynes-Cummings Model. *Phys. Rev. Lett.* **105**, 263603 (2010).

- ⁸ Günter, G. *et al.* Sub-cycle switch-on of ultrastrong lightmatter interaction. *Nature* **458**, 178–181 (2009).
- ⁹ Schwartz, T., Hutchison, J. A., Maali, A., Genet, C. & Ebbesen, T. W. Reversible Switching of Ultrastrong Light-Molecule Coupling. *Phys. Rev. Lett.* **106**, 196405 (2011).
- ¹⁰ Baumann, K., Guerlin, C., Brennecke, F. & Esslinger, T. Dicke quantum phase transition with a superfluid gas in an optical cavity. *Nature* **464**, 1301–1306 (2011).
- ¹¹ Dicke, R. H. Coherence in Spontaneous Radiation Processes. *Phys. Rev.* **93**, 99–110 (1954).
- ¹² Nakamura, Y., Pashkin, Yu. A. & Tsai, J. S. Coherent control of macroscopic quantum states in a single-Cooper-pair box. *Nature (London)* **398**, 786–788 (1999).
- ¹³ Clarke, J. & Wilhelm, F. K. Superconducting quantum bits. *Nature (London)* **453**, 1031–1042 (2008).
- ¹⁴ Devoret, M., Girvin, S. & Schoelkopf, R. Circuit-QED: How strong can the coupling between a Josephson junction atom and a transmission line resonator be? *Ann. Phys. (Leipzig)* **16**, 767–769 (2007).
- ¹⁵ Niemczyk, T. *et al.* Circuit quantum electrodynamics in the ultrastrong-coupling regime. *Nature Phys.* **6**, 772–776 (2010).
- ¹⁶ Forn-Diaz, P. *et al.* Observation of the Bloch-Siegert Shift in a Qubit-Oscillator System in the Ultrastrong Coupling Regime. *Phys. Rev. Lett.* **105**, 237001 (2010).
- ¹⁷ Ashhab, S. & Nori, F. Qubit-oscillator systems in the ultrastrong-coupling regime and their potential for preparing nonclassical states. *Phys. Rev. A* **81**, 042311 (2010).
- ¹⁸ Mooij, J. E. *et al.* Josephson Persistent-Current Qubit. *Science* **285**, 1036–1039 (1999).
- ¹⁹ Rabi, I. I. Space quantization in a gyrating magnetic field. *Phys. Rev.* **51(8)**, 652 (1937).
- ²⁰ Shimoda, K., Wang, T. C. & Townes, C. H. Further aspects of maser theory. *Phys. Rev.* **102**, 1308–1321 (1956).
- ²¹ Jaynes, E. T. & Cummings, F. W. Comparison of quantum and semiclassical radiation theories with application to the beam maser. *Proc. IEEE* **51**, 89–109 (1963).
- ²² Braak, D. Integrability of the Rabi Model. *Phys. Rev. Lett.* **107**, 100401 (2011).
- ²³ Bourassa, J. *et al.* Ultrastrong coupling regime of cavity QED with phase-biased flux qubits. *Phys. Rev. A* **80**, 032109 (2009).
- ²⁴ Rzążewski K., Wódkiewicz K. & Żakowicz W. Phase Transitions, Two-Level Atoms, and the A^2 Term. *Phys. Rev. Lett.* **35**, 432–434 (1975).

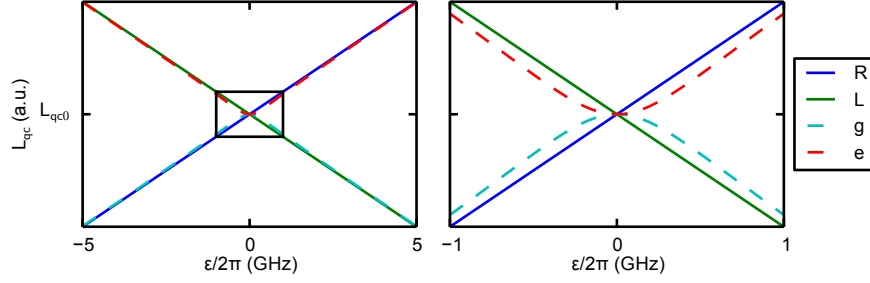
- ²⁵ Lamb, W. E. & Retherford, R. C. Fine structure of the hydrogen atom by a microwave method. *Phys. Rev.* **72(3)**, 241–243 (1947).
- ²⁶ Blais, A., Huang, R.-S., Wallraff, A., Girvin, S. M. & Schoelkopf, R. J. Cavity quantum electrodynamics for superconducting electrical circuits: An architecture for quantum computation. *Phys. Rev. A* **69**, 062320 (2004).
- ²⁷ Walls, D. F. & Milburn, G. J. *Quantum optics* (Springer Science & Business Media, 2007).
- ²⁸ Hopfield, J. J. Theory of the contribution of excitons to the complex dielectric constant of crystals. *Phys. Rev.* **112**, 1555–1567 (1958).



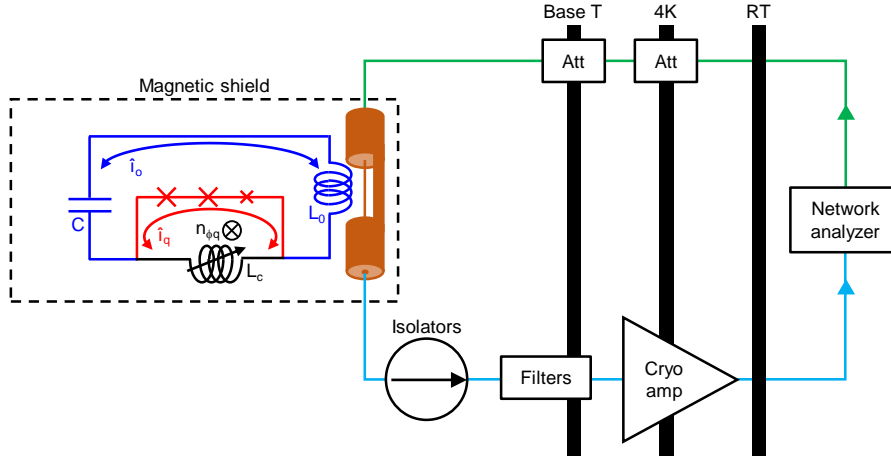
Extended Data Figure 1. **Circuit diagrams of the flux qubit and coupler.** **a**, The qubit (red and black) consists of three Josephson junctions in the upper branch (red) and the coupler (black), which is four parallel Josephson junctions. **b**, The coupler junctions are simplified to a single effective Josephson junction. **c**, The equivalent circuit of **b**, now consisting of the mutual inductance M and the inductance across the qubit and the coupler L_{qc} , which depends on both the flux bias and the qubit state.



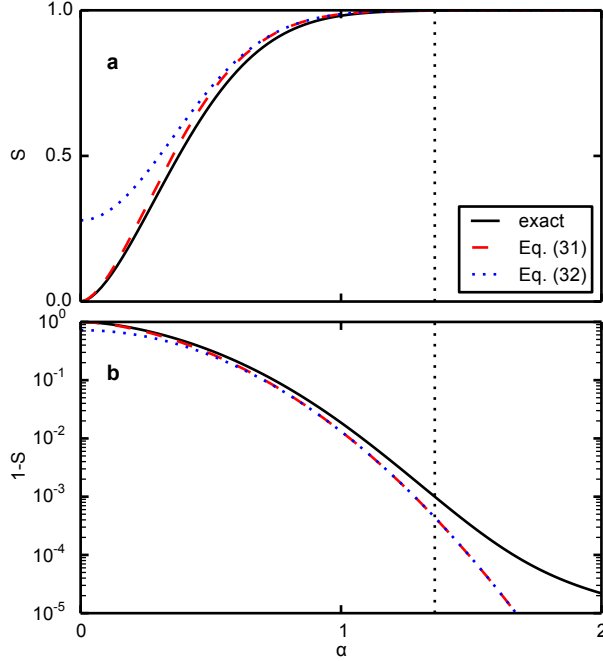
Extended Data Figure 2. **Flux bias dependence of phases and inductances.** **a**, The flux bias dependence of the phase across the different Josephson junctions in Extended Data Fig. 1b when the qubit state is $|L\rangle_q$ and $|R\rangle_q$. **b** (**c**), The flux bias dependence of the phase across the upper branch of the qubit loop ϕ_u at three different current bias values, $\delta I = 0, \pm 10$ nA, when the qubit state is $|L\rangle_q$ ($|R\rangle_q$). **d**, The flux bias dependence of the coupler inductance L_c , the mutual inductance M , and the inductance across the qubit and the coupler L_{qc} when the qubit state is $|L\rangle_q$ and $|R\rangle_q$.



Extended Data Figure 3. **Flux-bias and qubit-state dependences of L_{qc} .** The right panel is the magnification of the rectangle part of the left panel. The blue and green solid lines and the red and cyan dashed lines correspond to $L_{qc}^{|R\rangle}$, $L_{qc}^{|L\rangle}$, $L_{qc}^{|g\rangle}$, and $L_{qc}^{|e\rangle}$, respectively.



Extended Data Figure 4. **Measurement setup.** The sample of flux qubit coupled to the LC oscillator is cooled down in a dilution refrigerator and measured using a network analyser. For the sample details, see Fig. 1 in the main text. The green and cyan lines are the signal input and output lines, respectively.



Extended Data Figure 5. **The qubit-oscillator entanglement as a function of α .** The entanglement is calculated from Eq. (31) (red dashed line), Eq. (32) (blue dotted line), and a numerical diagonalization of the Rabi model Hamiltonian using the parameters Δ and ω_o from circuit II in our experiment (black solid line). Panel **a** shows the linear plot of S while panel **b** shows the log plot of $1 - S$. The black dotted line indicates the displacement of circuit II, i.e. $\alpha = 1.36$. Both Eq. (31) and Eq. (32) slightly overestimate the entanglement when $\alpha > 1.5$, where the entanglement is around 99.9% or higher. Since Eq. (32) is derived by assuming a large value of α , it is not valid when $\alpha < 0.5$.